Microfluidics and Nanofluidics (2022) 26:57
https://doi.org/10.1007/s10404-022-02563-x

RESEARCH PAPER

Transient flow patterns of start-up flow in round microcavities

Feng Shen[1,2] · Mingzhu Ai[1] · Siyu Zhao[1] · Chengjin Yan[1] · Zhaomiao Liu[1,2]

Received: 10 February 2022 / Accepted: 15 June 2022 / Published online: 7 July 2022

Abstract

Start-up flow from rest in cavities plays an important role in many related applications. In this study, flow visualization experiments were carried out to investigate the effects of Reynolds numbers ($Re=0$–266) and cavity aspect ratios (opening width/cavity diameter of 1.1, 1.3, 1.5 and 1.7) on developing separatrix morphologies in round microcavities. Three different separatrixes of dye solution appear successively and evolve with time at $Re=155$. To reveal the mechanism of separatrix formation and migration, the flow filed characteristics of developing vortex structures were quantitatively measured using micro-particle image velocimetry (micro-PIV) system. Three evolution modes of the separatrixes were mapped, which are determined by the combined effects of flow conditions, cavity aspect ratios and the cavity opening width in a complex way. The results could provide deep insights into the physics of fluid convection and mass transfer during the initial flow stage in round microcavities and guide the design of devices in related microfluidic applications.

Graphical abstract

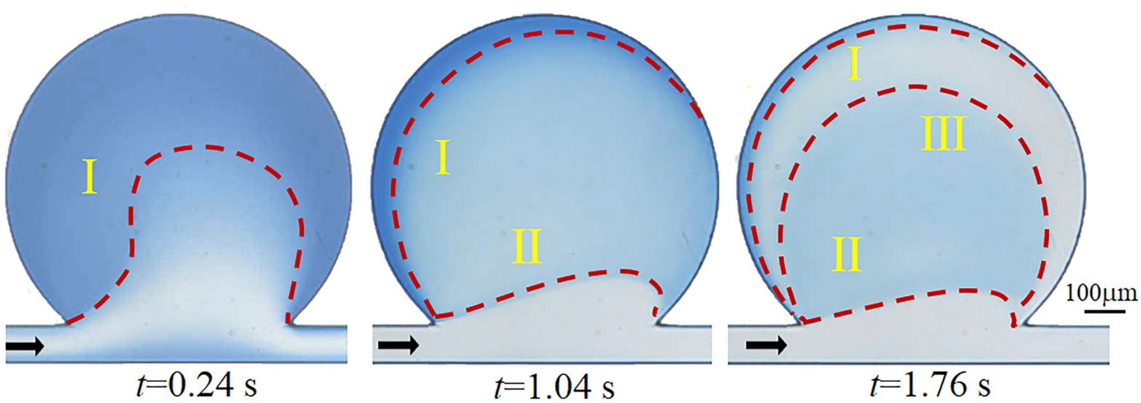

Evolution of three separatrixes in a round microcavity ($W_c=400$ μm and $e_c=1.7$ at $Re=155$)

Keywords Microfluidics · Start-up flow · Developing vortex · Transient flow · Microcavity

✉ Zhaomiao Liu
lzm@bjut.edu.cn

[1] Faculty of Materials and Manufacturing, Beijing University of Technology, Beijing 100124, China

[2] Beijing Key Laboratory of Advanced Manufacturing Technology, Beijing University of Technology, Beijing 100124, China

1 Introduction

Cavity flow featured by vortex is alway a research focus of fluid mechanics (Shankar and Deshpande 2000; Shelby et al. 2003; Heaton 2008; Zhu et al. 2022). Straight channel with cavity structures (i.e., groove, expansion–contraction) on side walls is a common flow configuration in nature and industry (Dudukovic et al. 2021; Nguyen et al. 2019; Sznitman 2022). Diversity of cavity shapes (e.g., rectangular, round and diamond shaped) have been employed in microfluidic or lab-on-a-chip system for many applications, e.g., flow control (Choi and Park 2010; Galie et al. 2014), fluid mixing and heat transfer (Fishler et al. 2013; Adachi et al. 2009) and particles/cells manipulations (Cho et al. 2018; Haddadi and Di Carlo 2017; Shen et al. 2021), where the cavity flow is in the steady state under stationary inlet flow conditions (Yu et al. 2005; Khabiry et al. 2009; Yew et al. 2013; Vrhovec et al. 2011; Osterman et al. 2016).

Start-up flow or initiation flow is a transient flow process, in which the flow starts from rest to be developed (Andersson and Holmedal 1995; Leal 2007). Since Szymanski (1932) first reported the concept of laminar initiation flow in a circular pipe, it has become a canonical problem and many studies devoted to solving its numerical solution (Patience and Mehrotra 1989; Yang and Zhu 2010). In recent years, the start-up flow in microscales has attracted the research attention (Klebinger et al. 2013; Kang et al. 2014; Martínez-Calvo et al. 2020). For example, Coelho et al. (2016) investigated the transient vortex structure in shale gaps in microscales to enhance the oil recovery rate. Using numerical modeling, Martínez-Calvo et al. (2020) investigated the start-up time and related influence parameters, finding that the flow needs more time to be fully developed in a shallow deformable microchannel. Zeitoun et al. (2014) found that the start-up flow would cause an energy loss on the flow rate, which should be considered for the design of microchannel networks. Shen et al. (2020) experimentally studied the effects of the Reynolds numbers ($Re < 116.9$) and cavity aspect ratio (length/width = 1, 3 and 5) on the vortex structure in the start-up flow in long rectangular microcavities, finding that the vortex structure evolves in a complex way.

The start-up flow in round cavities has been attracting increasing research attention (Horner et al. 2015; Galie et al. 2014; Vilkinis et al. 2016), as the round cavities can be used as simplified models to study the transient flow in alveoli and intracranial aneurysms (Lv et al. 2020; Epshtein and Korin 2018). For example, the transient flow pattern in alveoli, which evolves from attached flow to vortex flow can affect the development of embryonic lung (Tenenbaum-Katan et al. 2018; Dong et al. 2022). Moreover, as the human blood flow is pulsating, the hemodynamics in aneurysms are also inherently transient (Nguyen et al. 2019; Chassagne et al. 2021). However, the studies on the transient flow patterns in the start-up flow in round microcavities are few (Dong et al. 2022; Sznitman 2022). Understanding the background physics is an essential step toward revealing the effects of the fluid flow and mass transfer on relevant biological and chemical applications (Lv et al. 2020; Chassagne et al. 2021).

In this work, flow visualization experiments were carried out to reveal the evolution of the transient flow patterns of the start-up flow in round microcavities. Three separatrixes of dye solution were visualized, which evolved with time in a complex way. To reveal the background physics of separatrixes formation and migration, the flow velocity field vectors of the developing microvortices were quantitatively measured by using a micro-particle image velocimetry (micro-PIV). Three evolution modes of the dye flow pattern were identified, which are significantly different with that in rectangular cavities (Shen et al. 2020). Based on the Re (0–266) and cavity opening width/ diameter ratios ($e_c = 1.1$, 1.3, 1.5 and 1.7), the critical conditions for the transition of the evolution modes were characterized.

2 Methods

2.1 Microfluidic chip

The microfluidic chip used in the experiments consists of a straight microchannel ($W = H = 100$ μm), two inlet channels and four round microcavities (Fig. 1a). Three chips were designed, each with a fixed cavity opening width (W_c) of 300, 400 and 600 μm, respectively. The diameter of the cavity D_c changes according to the aspect ratios

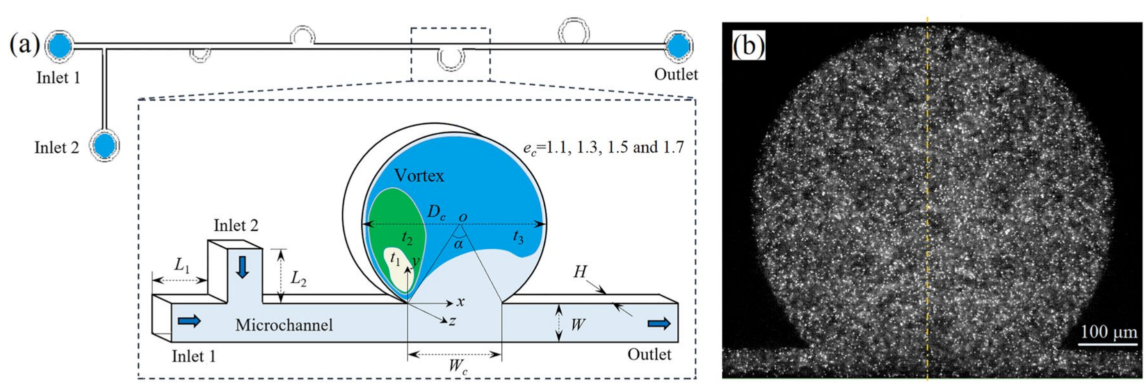

Fig. 1 **a** Schematic diagram of the microfluidic chip. **b** Snapshot of the tracer particles in a round microcavity

$$e_c = D_c / W_c, \tag{1}$$

which has four values of 1.1, 1.3, 1.5 and 1.7. For example, for W_c = 400 μm, the diameters of the four microcavities are D_c = 440, 520, 600 and 680 μm. The opening angle of the cavity mouth is defined as $\alpha = 2\arcsin(1/e_c)$, which has four values and affects the flow patterns significantly (Fishler et al. 2013). The microcavity depth is also 100 μm. The total length of the microchannel is 42 mm, and the lengths of both inlet channels are $L_1 = L_2 = 6$ mm. The distance from inlet 2 to the first microcavity is 5 mm, while the distance between each microcavity is fixed at 6 mm. The microfluidic chip was made of polydimethylsiloxane (PDMS) using soft lithography techniques. The coordinate system of the microcavities is shown in Fig. 1a and the origin is fixed at the leading edge of the cavity. The dimensionless position of the vortex core in the microcavity is defined as

$$x^* = x/H \text{ and } y^* = y/H. \tag{2}$$

2.2 Experimental setup

In the dye flow visualization experiments, a high-speed microscopic imaging system (Keyence, VW-9000) was employed, which consists of a 100× zoom lens and a high-speed camera (resolution of 640×480 pixels). At first, methylene blue solution 1.0% (*w*/*v*) in water was injected from inlet 2. When the cavities were fully filled with the dye solution, the inlet 2 was closed. Then, after 90 s, deionized water ($\rho = 998.2$ kg/m^3 and $\mu = 10^{-3}$ Pa · s) was injected from the inlet 1 at a fixed flow rate. Two syringe pumps (Harvard Apparatus, PHD2000) were used for the fluid injection. The dye flow patterns were captured at a rate of 1000 frames per second (fps).

In the flow measurement experiments, the micro-PIV system (Dantec Dynamics) includes a double-pulse 532-nm Nd: YAG laser, a high-speed double frame CCD camera (12 bit, 70% quantum efficiency, 1344×1024 pixels), an inverted Leica microscope, a signal synchronizer and a computer with a PIV software. Details of the micro-PIV system are described in our previous studies (Shen et al. 2015, 2018). Moreover, the test fluid is water, which is seeded with polystyrene red fluorescent particles (diameter of 860 nm, density of 1.03 g/cm^3, Duke Scientific). Tween 20 (0.3% v/v) is added to the water. A 10× objective lens with NA = 0.25 was used and tracer particles in the *x*–*y* plane at the mid-depth of the cavity were captured (Fig. 1b). There are about 10–16 particles in an interrogation area of a 32×32 pixels window. Image pairs of particles were acquired on a double-frames mode with a frequency of 12 fps, and the interval time varies from 50 to 200 μs according to the flow rate. The adaptive cross-correlation (ACC) algorithm was employed to analyze the image pairs (Wereley and Meinhart 2001). The measurement error is below 3.5%. At last, the results were post-processed using TECPLOT software. For the measured cavity, the experiments number is more than 20 times and the results are rearranged in chronological order. The inlet flow rate is characterized by the Reynolds number,

$$Re = \rho U D_h / \mu, \tag{3}$$

where ρ, μ, and U are the fluid density, dynamic viscosity and average velocity in the microchannel, respectively. $D_h = 2WH/(W+H)$ is the hydraulic diameter of the microchannel. The Re ranges from 0 to 266. The velocities (u and v) can be nondimensionalized as

$$u^* = u/U \text{ and } v^* = v/U. \tag{4}$$

For start-up flow in circular tube, the tube radius is selected as the characteristic length scale (Leal 2007), however, for the cavity configuration, we define the characteristic length scale as

$$l_c = D_c^2 / \sqrt{W_c \times H}. \tag{5}$$

Therefore, in the start-up process, the characteristic time scale is defined as Leal (2007)

$$t_c = l_c^2 / \upsilon, \tag{6}$$

where ν is the fluid kinematic viscosity. t_c is proportional to the time period over which the cavity flow evolves from the rest to the final steady state. For example, in the cavity with W_c = 400 μm, e_c = 1.7, the calculated t_c is 5.345 s. Using the natural time (t), the dimensionless time can be calculated as.

$$t^* = t/t_c. \tag{7}$$

3 Results and discussion

3.1 Transient dye flow patterns

The developing process of dye flow patterns in a round microcavity (W_c = 400 μm, e_c = 1.7) at Re = 155 is shown in Fig. 2 and Video 1 (see the Supplementary Material). Three separatrixes appear successively in the cavity flow field. According to their morphologies, we define separatrix I as the boundary between the water flow and the remaining dye solution in the cavity. Separatrix II is the boundary between the vortex and the microchannel flow, while separatrix III is the boundary between a water jet and the vortex. Their morphologies evolve rapidly with time in different ways. When the water arrives at the cavity leading edge, time is set as $t^* = 0$ (Fig. 2a). At first, separatrix

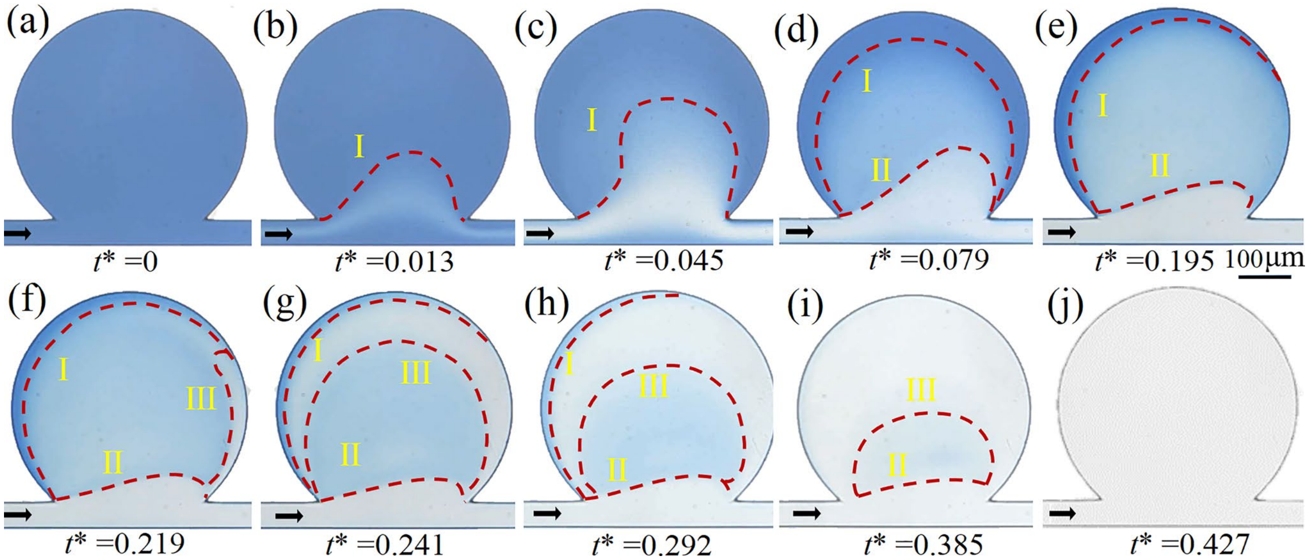

Fig. 2 Evolution of three separatrixes in a microcavity with $W_c = 400$ μm, $e_c = 1.7$ at $Re = 155$. (Movie 1 in the online supplementary data at https://doi.org/8888). Water flows from left to right and flushes the dye out

I appears in the cavity entrance at $t^* = 0.013$ (Fig. 2b) and then migrates quickly into the deep region of the cavity at $t^* = 0.045$ (Fig. 2c). Meanwhile, the color of the fluid in the cavity center becomes light gradually. Induced by the three-dimensional flow structure and dye diffusion, separatrix I becomes a little bit murky. Therefore, we speculate that dye near the upper and lower cavity walls is almost static in the initial stage of the start-up flow.

At $t^* = 0.079$, separatrix I moves to the vicinity of the cavity round bottom and becomes symmetrical about the centerline (Fig. 2d). Meanwhile, separatrix II appears on the upper side region of the entrance, which morphology is relatively distinct. At $t^* = 0.195$, separatrix I becomes unsymmetrical and migrates towards the left side of the cavity. On the contrary, separatrix II moves towards the entrance (Fig. 2e). We speculate that a small vortex generates near the leading edge, which expands its size continuously, leading to the evolutionary way of the two separatrixes. The vortex hindered the convection and mass transfer between the cavity and the main channel.

Interestingly, separatrix III appears near the trailing edge of the cavity at $t^* = 0.219$ (Fig. 2f). Then, it migrates along the cavity bottom towards the left side of the cavity (Fig. 2g), flushing the separatrix I away. Then, at $t^* = 0.292$, the flow region between the separatrixes III and I expands with color becoming light (Fig. 2h). The phenomena were observed for the first in this study, which are different from that in rectangular microcavities (Shen et al. 2020). The formation of separatrix III results from the injection of a high-speed water jet through a small gap between the end of the separatrix II and the trailing wall. The water jet is separated from the curved boundary of the main channel flow. At $t^* = 0.385$, separatrix I disappears, while the flow region between the separatrixes II and III, where is the vortex core, shrinks gradually (Fig. 2i). A little bit of dye solution is still trapped in the vortex core area. At last, all the three separatrixes disappear at $t^* = 0.427$. The results demonstrate that the water jet plays an important role in the fluid flow and mass transfer between the microchannel and the cavity in the start-up flow. Please note that the transient flow patterns occur under a steady flow condition (at a fixed inlet flow rate). Although many studies have been devoted to characterizing the fluid flow and mass transfer in cavities, most of the research focus on flow patterns in steady state (Yew et al. 2013; Fishler et al. 2013). As start-up flow exists widely in nature and industry in practice, it is meaningful to understand the transient flow behaviors.

3.2 Micro-PIV results of developing vortex

Figure 3 shows the micro-PIV results of the flow field in the same cavity ($W_c = 400$, $e_c = 1.7$) at $Re = 155$. According to the flow field structure, we define three flow forms in the round cavity, i.e., attached, transitional and developed (or vortex) flows. In the beginning, driven by the microchannel flow, fluid in the cavity entrance region starts up to flow from rest. Then, fluid in all the cavity region starts to flow at a very low speed at $t^* = 0.045$ (Fig. 3a). During this stage, the cavity flow is laminar and the channel flow can affect the deep region of the cavity, which flow form is attached. However, as the duration time of this stage is instantaneous, only dye near the entrance is flushed out, leading to the occurrence of separatrix I (Fig. 2a).

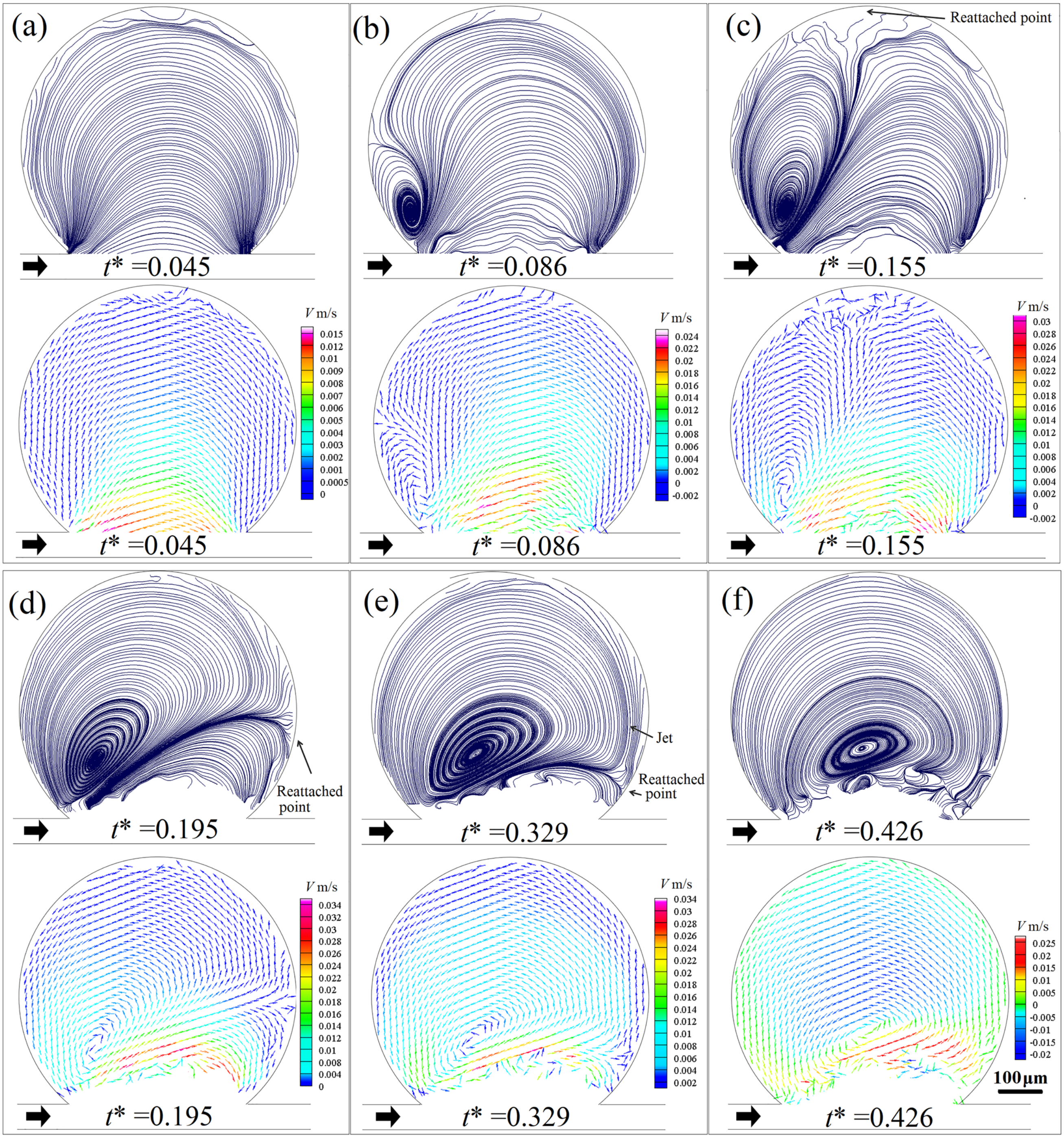

Fig. 3 Micro-PIV results of the streamlines and velocity vector fields of the developing vortex in the round microcavity ($W_c = 400$ μm, $e_c = 1.7$ at $Re = 155$)

Then, a small vortex generates near the leading edge at $t^* = 0.086$ (Fig. 3b). The generation of the small vortex is resulted from the sudden expansion of the microchannel, which causes the separation of the boundary layer (Yu et al. 2005; Fishler et al. 2013). At $t^* = 0.155$, the vortex expands its size quickly (Fig. 3c). Please note that there is a reattached point of the vortex on the cavity bottom. At $t^* = 0.195$, with the vortex area expanding, the reattached point moves to the right side of the cavity bottom (Fig. 3d). The boundary streamline of the vortex and microchannel flow migrates towards the entrance, which trend is identical with the movement of separatrix II (Fig. 2). In this stage, the cavity flow develops into transitional flow (Fig. 3b–d). Confined by the boundary, the dye is trapped into the vortex and mass transfer become inhibited.

At $t^*=0.329$, the vortex area expands and nearly occupies the whole cavity with intensity increasing (Fig. 3e), which is the developed flow. Meanwhile, the reattached point nearly reaches the cavity trailing edge, and a high-speed jet flow generates, which is separated from the boundary streamlines of the microchannel flow. This is the reason for the phenomenon that the flow region between separatrixes I and III is filled with water jet in Fig. 2 g–h. We infer that the jet flow is caused by the confinement of the trailing cavity wall and the fluid inertia. At $t^*=0.426$, the vortex occupies the whole cavity region (Fig. 3f). Moreover, as the velocity of the vortex is two orders of magnitude lower than that of the main channel (Shen et al. 2015), only the cavity flow region was measured in the experiments. Please note that the vortex structures are transient and developing, which are different from the flow in circular microcavities (Fishler et al. 2013). The results show that the developing vortex structure causes the complex morphologies of the separatrixes. Moreover, the three flow forms are instantaneous and inherently different from that the steady-state flow in rectangular microcavities reported in our previous study (Shen et al. 2015). Furthermore, through the comparison of Figs. 2 and 3, we speculate that there is a relatively high-speed flow area in the vortex region, which is between the cavity bottom and vortex core and dominates the fluid flow and mass transfer in the vortex.

3.3 Evolution of vortex core and velocity distribution

To further reveal the vortex evolution process, the position of the vortex core at each time was extracted. Figure 4a shows that the migration trajectory of the vortex core with time ($Re=155$, $e_c=1.7$, $W_c=400$). At $t^*=0.086$, the vortex core is near the leading edge of the entrance ($x^*=-0.25$ and $y^*=1.05$). It first moves along the y-direction until at $t^*=0.155$ at $x^*=-0.24$ and $y^*=1.53$, and then toward the right and deep part of the cavity until at $t^*=0.426$ at $x^*=1.68$ and $y^*=2.25$. Although the vortex core is in the left part of the cavity ($x^*<2.0$), the vortex area expands continuously and occupies the whole cavity.

The velocity distributions along the transversal and longitudinal lines across the vortex core are extracted, as shown in Fig. 4b, c. In the vortex core, the flow velocities are nearly zero. It can be found that the velocity distributions change acutely with time. At t_1^*, the v-velocity is very low, while the u-velocity decreases from 9 mm/s to nearly 0. On the contrary, at t_2^*, the v-velocity becomes high with a peak of up to 27 mm/s, while the u-velocity is relatively low, which means that the vortex area is small, and the microchannel flow dominates the cavity flow at this moment. From t_3^* to t_5^*, as the vortex area expands, the vortex core moves towards the cavity centerline.

The v-velocity on the left side of the vortex core increases in the negative direction of the y-axis, while that on the right side of the vortex core first increases and then decreases in the positive direction of the y-axis. The negative peak increases while the positive peak decreases with time. At t_5^*, the v-velocity distribution becomes symmetrical about the position of the vortex core ($x^*=1.68$). From t_3^* to t_5^*, the u-velocity first increases to a positive peak rapidly, next decreases exponentially to 0 and then increases to a negative peak with flow direction reversal, at last it decreases to 0 again gradually. The positive peak is caused by the microchannel flow. Both the positive and negative peaks increase over time due the enhancement of the vortex intensity. The trends of the u and v-velocities at t_5^*, are nearly identical with that of developed flow in the circular microcavity (Fishler et al. 2013).

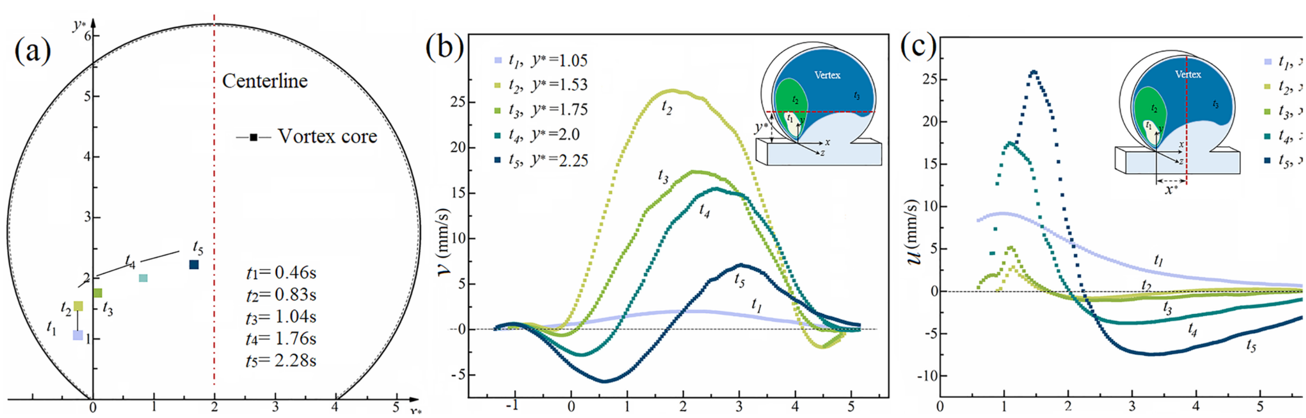

Fig. 4 **a** Migration of the location of the vortex core with time. **b** v-velocity distributions along the transversal lines across the vortex core. **c** u-velocity distributions along the longitudinal line across the vortex core ($Re=155$, $e_c=1.7$, $W_c=400$ μm)

3.4 Effect of Re on dye flow patterns

The effect of the *Re* on the evolution of the dye flow patterns in the cavity with $W_c = 600$ μm and $e_c = 1.5$ was also investigated, as shown in Fig. 5. According to the morphology of the separatrixes, the evolution of the dye flow patterns in the start-up flow can be classified into three modes. At $Re = 33.3$, only separatrix I appears and migrates towards the round bottom of the cavity with time, which phenomenon is classified as mode I (Fig. 5a). We speculate the reason is that the cavity flow is attached, where the microchannel flow can reach the deep region of the cavity and flush the dye solution away.

For mode II, separatrixes I and II appear in the entrance region at $Re = 66.6$ (Fig. 5b). Separatrixes I migrates towards the deep region of the cavity, while separatrix II remains near the entrance until its disappearance. This phenomenon is different from that in Fig. 2d, e, where the separatrix II moves towards the entrance. We speculate that the reason is that the flow form is transitional, where the vortex size is relatively small and can only occupy the left region of the cavity. Therefore, water from the microchannel can flow into the right region of the cavity and flush the dye out. At $t^* = 0.228$, separatrix II disappear, while separatrix I remains in the upper right region of the cavity bottom.

For mode III, all three separatrixes successively appear in the cavity at $Re = 111$ and 178. On the contrary, separatrix I moves towards the upper left region of the cavity bottom. Driven by the water jet, separatrix III appears near the trailing wall and the developed vortex traps the dye in the core

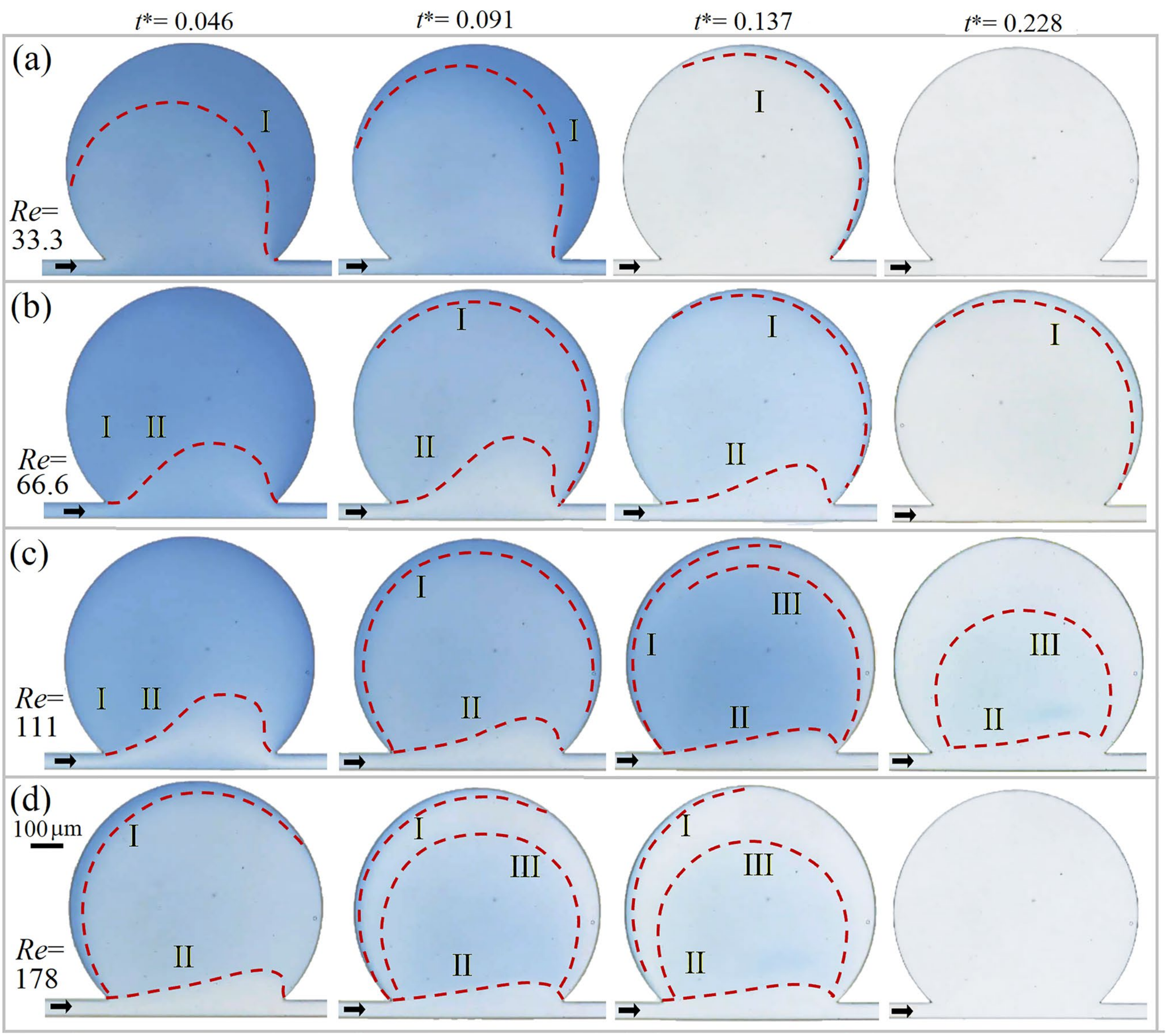

Fig. 5 Evolution of the dye flow patterns in the microcavity with $W_c = 600$ μm and $e_c = 1.5$. **a** $Re = 33.3$; **b** $Re = 66.6$; **c** $Re = 111$; **d** $Re = 178$

area. The evolution process of the dye flow patterns is similar with that in Fig. 2. Moreover, due to the inhibiting effect, the duration time for the main channel flow to flush the dye out of the cavity (or the evolution period of the flow patterns) is shorter at $Re = 33.3$ (Fig. 5a) than that at $Re = 111$ (Fig. 5c). At $Re = 178$, however, the duration time decreases (Fig. 5d). The results can provide theoretical guidance for relevant applications, such as cavity cleaning, fluid convection and material exchange in cavity-based structures.

3.5 Effect of cavity aspect ratio on dye flow patterns

Figure 6 shows the evolution of dye flow patterns in cavities with different aspect ratios at $Re = 155$. In the cavity with $e_c = 1.1$ (Fig. 6a), the evolution of the dye flow pattern is in mode I, where only separatrix I appears at $t = 0.12$ s and then moves towards the bottom of the cavity. At $t = 0.71$ s, the dye has been flushed out and the cavity flow becomes steady. In the cavity with $e_c = 1.3$ (Fig. 6b), evolution mode II occurs. The separatrix II is transient stable at $t = 0.44$ s until it disappears. In the cavity with $e_c = 1.7$ (Fig. 6c), evolution mode III occurs, which is very similar to that in Fig. 2. However, due to the small opening width ($W_c = 300$ μm), the water jet appears at $t = 1.04$ s in Fig. 6c, which is earlier than $t = 1.17$ s in Fig. 2f.

It can be found that with the e_c increasing, the evolution process becomes more complex, changing from mode I to II and then to III with the increase of the duration period. Please note that the mode transform in Fig. 6 is caused by the e_c. According to our previous study (Shen et al. 2018), it is easier for the flow to be developed in small cavities. Therefore, we speculate that the final flow in the three cavities are all developed. The results show that the e_c has significant effects on the evolution of the dye flow patterns.

3.6 Map of evolution modes

To guide the design of microfluidic devices, we mapped the three evolution modes as a function of the control parameters Re (0–266) and e_c (1.1–1.7), as shown in Fig. 7a–c. It can be found that the transition between modes II and III (line I) decreases linearly as e_c increases, while the transition between modes I and II first decreases rapidly ($e_c = 1.1$–1.3) then slowly ($e_c = 1.3$–1.7). The critical Re_c for the occurrence of mode III is higher than that of mode II in the same cavities. Moreover, as W_c increases from 300 to 600 μm,

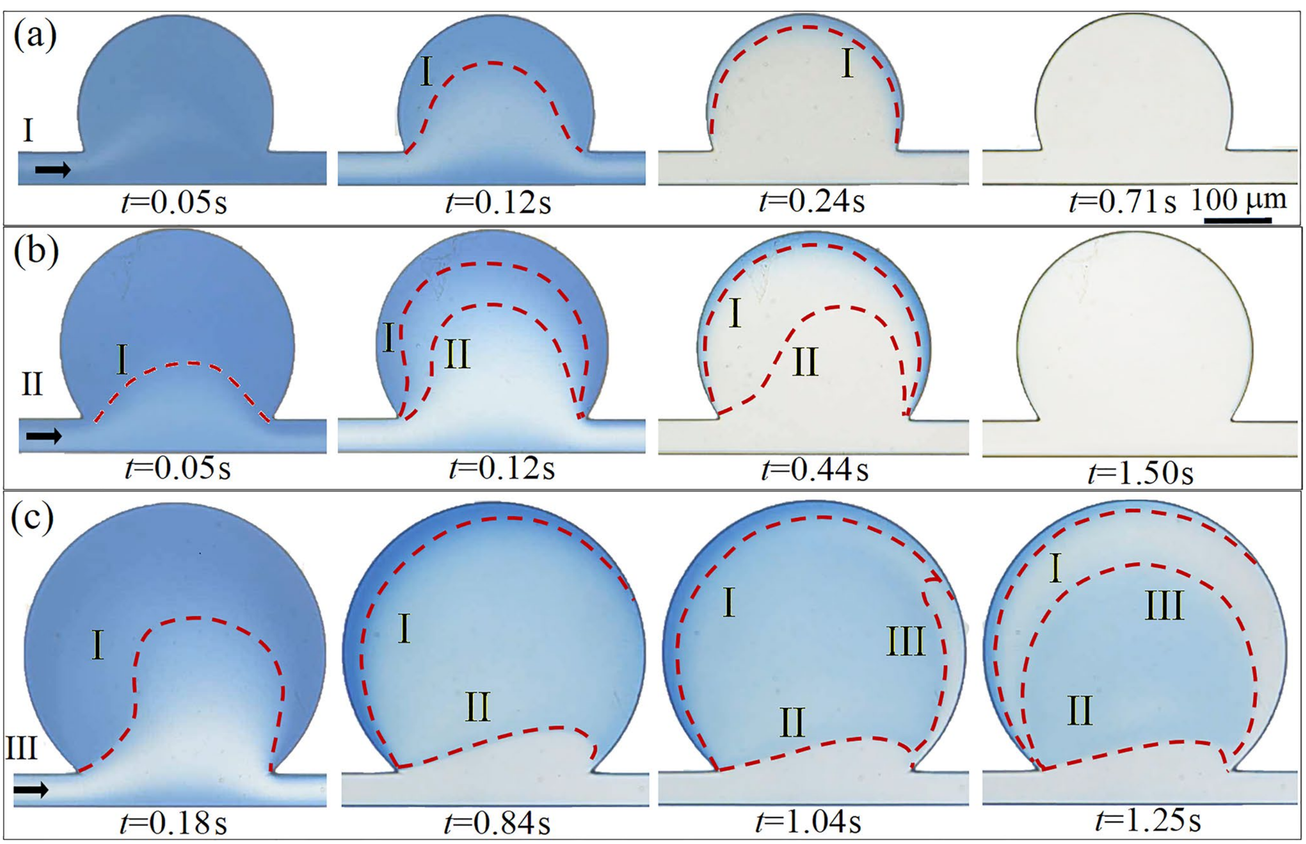

Fig. 6 Effect of aspect ratios on the transient dye flow patterns in different cavities with $W_c = 300$ μm at $Re = 155$; **a** Mode I ($e_c = 1.1$); **b** Mode II ($e_c = 1.3$); **c** Mode III ($e_c = 1.7$)

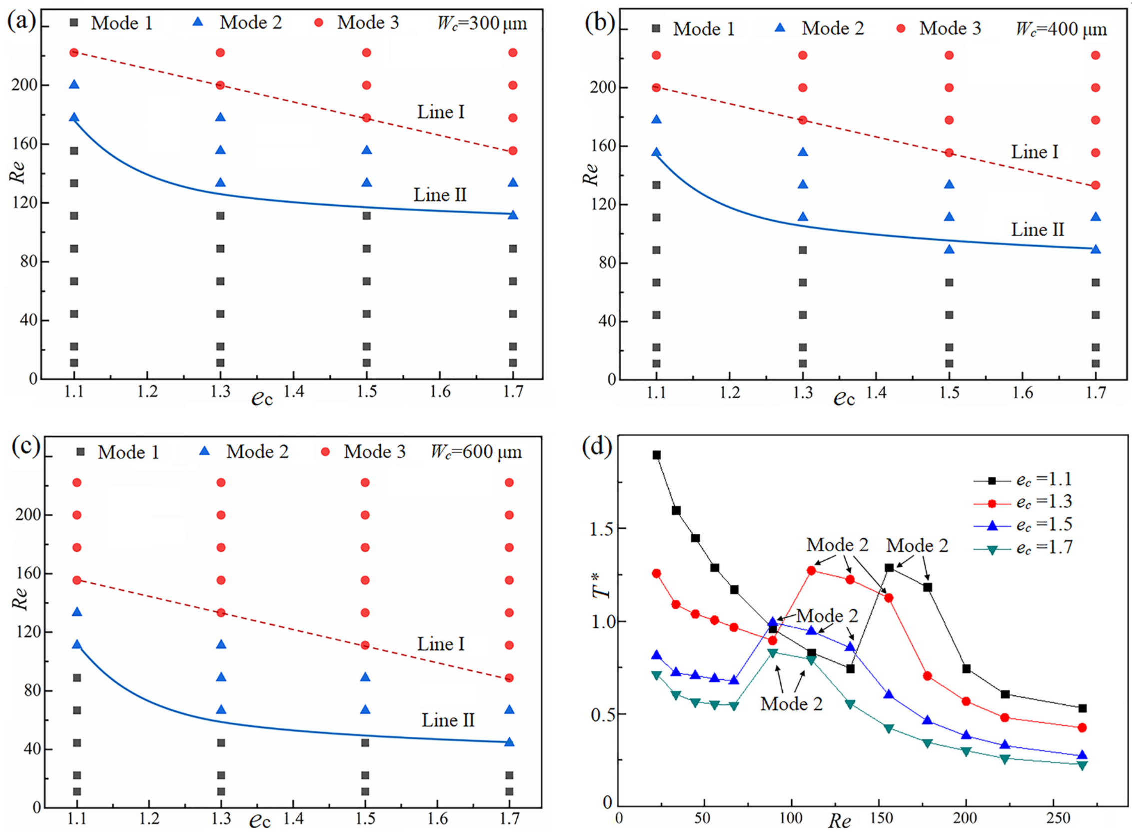

Fig. 7 Maps for evolution modes based on the Re–e_c in cavities with **a** $W_c = 300$ μm, **b** $W_c = 400$ μm and **c** $W_c = 600$ μm. **d** Dimensionless start-up time (T^*) in cavities with $W_c = 400$ μm

the corresponding Re_c for the transition between the modes decreases. The results indicate that the dye is easier to be discharged and the mass exchange becomes easier in the cavity with a large opening width.

The duration time or start-up time (T), referring to the time required for the fluid system in the cavity to develop from rest to the steady state (the dye is thoroughly flushed out), is an important parameter in the flow developing process and nondimensionalized as $T^* = T/t_c$. Figure 7d shows the relationships between T^* and Re (0–266) in cavities with different aspect ratios ($W_c = 400$ μm). It can be found that the curves decrease gradually with Re increase, but there is still a peak in each curve. For example, in the cavity with $e_c = 1.1$, T^* deceases from 1.899 s to 0.747 s as the Re increases from 22 to 133. At $Re = 155$, T^* reaches its peak value of 1.291 and then decreases gradually to 0.534 s at $Re = 266$. The peak is induced by the occurrence of the mode II in the cavity, where dye is trapped in a small vortex. When $Re > 178$, the evolution changes from mode II to mode III and the water jet helps to flush the remaining dye out. It can be inferred that the evolution mode experiences three modes as Re increases. Moreover, the absolute start-up time increases with the e_c increasing for a certain Re, which means that flow in a deeper cavity needs more time to be steady.

4 Conclusions

Flow visualization experiments were carried out to reveal the transient dye flow patterns and developing vortex structures of the start-up flow in round microcavities. Three separatrixes appear and evolve in a complex way in the flow field of the cavity ($W_c = 400$ μm, $e_c = 1.7$) at $Re = 155$. The micro-PIV results of the developing vortex indicate that the cavity flow experiences three flow forms, i.e., attached, transitional and developed, which are instantaneous and different from that of steady-state flow in cavities. The vortex core location and velocity distribution in the vortex have also been quantitatively measured. According to the separatrix morphology, three evolution modes of the dye flow pattern have been classified. To the best of our knowledge, the complicated morphological evolution of these three separatrixes in the start-up flow in a round microcavity was observed for the first time in this study, which are significantly different with that in rectangular microcavities. Both Re and e_c have significant effects on the evolution modes, which are determined by the combined effects of the cavity flow, dye diffusion and wall confinement. Moreover, maps of the transition of the evolution modes have been constructed based on *Re* and e_c. Furthermore, the relationships between the dimensionless start-up time and *Re* in cavities ($W_c = 400$ μm) with different e_c have been characterized. The results could deep the understanding of the physics of transient flow behaviors in round microcavities and provide useful design guidelines of microfluidic devices for relevant studies.

Supplementary Information The online version contains supplementary material available at https://doi.org/10.1007/s10404-022-02563-x.

Acknowledgements This work is supported in part by the National Natural Science Foundation of China (Nos. 11872083 and 12172017), Project of Beijing Municipal Education Commission (Nos. KZ202210005006 and KZ202110005007).

Declarations

Conflict of interest The authors declare that they have no known competing for financial interests or personal relationships that could have appeared to influence the work reported in this paper.

References

Adachi T, Tashiro Y, Arima H, Ikegami Y (2009) Pressure drop characteristics of flow in a symmetric channel with periodically expanded grooves. Chem Eng Sci 64:593–597
Andersson HI, Holmedal LE (1995) Start-up flow in a porous medium channel. Acta Mech 113:155–168
Chassagne F, Barbour MC, Chivukula VK, Machicoane N, Kim LJ, Levitt MR, Aliseda A (2021) The effect of Dean, Reynolds and Womersley numbers on the flow in a spherical cavity on a curved round pipe. Part 1. Fluid mechanics in the cavity as a canonical flow representing intracranial aneurysms. J Fluid Mech 915:A123
Cho H, Kim J, Song H, Sohn KY, Jeon M, Han KH (2018) Microfluidic technologies for circulating tumor cell isolation. Analyst 143:2936–2970
Choi S, Park JK (2010) Microfluidic rheometer for characterization of protein unfolding and aggregation in microflows. Small 6:1306–1310
Coelho JK, Pena MD, Romero OJ (2016) Pore-scale modeling of oil mobilization trapped in a square cavity. IEEE Lat Am Trans 14:1800–1807
Dong J, Yang Y, Zhu Y (2022) Recent advances in the understanding of alveolar flow. Biomicrofluidics 16:021502
Dudukovic NA, Fong EJ, Gemeda HB, Deotte JR, Duoss EB (2021) Cellular fluidics. Nature 595:58–65
Epshtein M, Korin N (2018) Mapping the transport kinetics of molecules and particles in idealized intracranial side aneurysms. Sci Rep 8:8528
Fishler R, Mulligan MK, Sznitman J (2013) Mapping low-Reynolds-number microcavity flows using microfluidic screening devices. Microfluid Nanofluid 15:491–500
Galie PA, Nguyen DHT, Choi CK, Cohen DM, Janmey PA, Chen CS (2014) Fluid shear stress threshold regulates angiogenic sprouting. PNAS 111:7968–7973
Haddadi H, Di Carlo D (2017) Inertial flow of a dilute suspension over cavities in a microchannel. J Fluid Mech 811:436–467
Heaton CJ (2008) On the appearance of Moffatt eddies in viscous cavity flow as the aspect ratio varies. Phys Fluids 20:103102–103111
Horner M, Metcalfe G, Ottino JM (2015) Convection-enhanced transport into open cavities, effect of cavity aspect ratio. Cardiovasc Eng Tech 6:352–363
Kang C, Roh C, Overfelt RA (2014) Pressure-driven deformation with soft polydimethylsiloxane (PDMS) by a regular syringe pump: challenge to the classical fluid dynamics by comparison of experimental and theoretical results. RSC Adv 4:3102–3112
Khabiry M, Chung BG, Hancock MJ, Soundararajan HC, Du Y, Cropek D, Lee WG, Khademhosseini A (2009) Cell docking in double grooves in a microfluidic channel. Small 5:1186–1194
Klebinger U, Wunderlich B, Bausch A (2013) Transient flow behavior of complex fluids in microfluidic channels. Microfluid Nanofluid 15:533–540
Leal LG (2007) Advanced transport phenomena: fluid mechanics and convective transport processes. Cambridge University Press
Lv H, Dong J, Qiu Y, Yang Y, Zhu Y (2020) Microflow in a rhythmically expanding alveolar chip with dynamic similarity. Lab Chip 20:2394–2402
Martínez-Calvo A, Sevilla A, Peng GG, Stone HA (2020) Start-up flow in shallow deformable microchannels. J Fluid Mech 885:A25
Nguyen N, Thurgood P, Arash A, Pirogova E, Baratchi S, Khoshmanesh K (2019) Inertial microfluidics with integrated vortex generators using liquid metal droplets as fugitive ink. Adv Funct Mater 29:1901998
Osterman N, Derganc J, Svenšek D (2016) Formation of vortices in long microcavities at low Reynolds number. Microfluid Nanofluid 20:33
Patience GS, Mehrotra AK (1989) Laminar start-up flow in short pipe lengths. Can J Chem Eng 67:883–888
Shankar PN, Deshpande MD (2000) Fluid mechanics in the driven cavity. Annu Rev Fluid Mech 32:93–136
Shelby JP, Lim DSW, Kuo JS, Chiu DT (2003) Generation of ultra-high radial accelerations in microvortices. Nature 425:38
Shen F, Xiao P, Liu Z (2015) Microparticle image velocimetry (μPIV) study of microcavity flow at low Reynolds number. Microfluid Nanofluid 19:403–417
Shen F, Xu M, Zhou B, Wang Z, Liu Z (2018) Effects of geometry factors on microvortices evolution in confined square microcavities. Microfluid Nanofluid 22:36
Shen F, Yan C, Li M, Liu Z (2020) Experimental study of transient behaviors of start-up flow in long microcavities. Chem Eng Sci 219:115591
Shen F, Li Z, Ai M, Gao H, Liu Z (2021) Round cavity-based vortex sorting of particles with enhanced holding capacity. Phys Fluids 33:082002
Sznitman J (2022) Revisiting airflow and aerosol transport phenomena in the deep lungs with microfluidics. Chem Rev 122:7182–7204
Szymanski G (1932) Quelques solutions exactes des equations der hydrodynamique du fluide visquex dans le case d'un tube cyiindrique. J Math Pures Et Appl 11:67–108
Tenenbaum-Katan J, Artzyschnirman A, Fishler R, Korin N, Sznitman J (2018) Biomimetics of the pulmonary environment in vitro: a microfluidics perspective. Biomicrofluidics 12:042209
Vilkinis P, Valantinavicˇius M, Pedišius N (2016) Investigation of fluid flow structure in open type cavity under stationary and pulsatile flow conditions. Energetika 62:37–44
Vrhovec S, Kavcic B, Mally M, Derganc J (2011) A microfluidic diffusion chamber for reversible environmental changes around flaccid lipid vesicles. Lab Chip 11:4200–4206
Wereley ST, Meinhart CD (2001) Second-order accurate particle image velocimetry. Exp Fluids 31:258–268

Yang D, Zhu K (2010) Start-up flow of a viscoelastic fluid in a pipe with a fractional Maxwell's model. Comput Math Appl 60:2231–2238

Yew AG, Pinero D, Hsieh AH, Atencia J (2013) Low Peclet number mass and momentum transport in microcavities. Appl Phys Lett 102:084108

Yu ZTF, Lee YK, Wong M, Zohar Y (2005) Fluid flows in microchannels with cavities. J Microelectromech Syst 14:1386–1398

Zeitoun RI, Langelier SM, Gill RT (2014) Implications of variable fluid resistance caused by start-up flow in microfluidic networks. Microfluid Nanofluid 16:473–482

Zhu G, Zhang Z, Shi X, Tan W (2022) Experimental study on inertial focusing pattern in asymmetric contraction–expansion array microchannel. Microfluid Nanofluid 26:1–11